PERGAMON

International Journal of Multiphase Flow 26 (2000) 1707–1736

International Journal of Multiphase Flow

www.elsevier.com/locate/ijmulflow

Numerical simulation of dilute turbulent gas–solid flows

C.K.K. Lun

Center for Multiphase Flows Research, 55 Cairnside Crescent, Toronto, Ont., Canada M2J 3M9

Received 15 October 1998; received in revised form 5 October 1999

Abstract

A new dilute turbulent gas–solid two-phase flow model in the grain inertia flow regime is developed in the present study. A set of time-averaged conservation equations for mass and momentum, and a two-equation multiscale k–ω closure are derived. The solid phase is composed of inelastic, frictional, uniform spheres. Each Lagrangian solid particle is tracked by integrating the particle equations of translational and rotational motion. The couplings in volume fraction, momentum and kinetic energy between the fluid and the solid phases are incorporated in this model. Turbulence modulation due to the solid particles is formulated on the basis of experimental observations. Interparticle collisions and particle–wall collisions are emulated by using a sticking–sliding collision model. The two-phase model is applied to study the steady state flow in a vertical pipe. Depending upon the particle size, mass loading and bulk carrier-fluid velocity, the two-phase system can experience turbulence attenuation, or augmentation, or a combination of both. In general, good agreement is found between the simulation prediction and the experimental data for the mean fluid and solid velocities. Furthermore, there is reasonable qualitative agreement for the fluid turbulence kinetic energy between the two. Many interesting numerical results for macroscopic flow properties of both fluid and solid phases are reported in this paper.

Keywords: Gas–solid suspension; Turbulence modulation; Stresses; Collisions; Dissipation

1. Introduction

Depending upon the particle Reynolds number, the solid concentration, the rate of deformation, the material properties of the fluid and the solid particles, various regimes of two-phase flows can be generated. For the case of low particle Reynolds number and dilute concentration, the fluid phase plays a major role in determining the dynamics of the system. This viscous flow regime has been investigated by a number of researchers, and the subject is

0301-9322/00/$ - see front matter
PII: S0301-9322(99)00106-8

relatively well understood. However, our understanding of the grain-inertia flow regime is still much more primitive, despite the vast number of applications found in industries and natural sciences. Recent reviews on the subject are available; for example, Crowe et al. (1996), Elghobashi (1994) and Jackson (1993).

Tsuji et al. (1984), Lee and Durst (1982) and Maeda et al. (1980) utilized the laser Doppler technique to measure the distributions of air–solid two-phase flow properties, such as mean fluid velocity, streamwise turbulence intensity, and mean solid particle velocity in air–solid two-phase flows inside vertical pipes. These experiments demonstrated some of the fundamental behavior of gas–solid suspensions.

Lun and Liu (1997) employed numerical simulations to study the dilute turbulent gas–solid flows in the grain-inertia regime in horizontal channels. The model incorporated couplings in volume fraction and momentum between the two phases, and an anisotropic k–ε two-equation closure. Many interesting flow properties were obtained from the simulations; for example grain stresses, granular temperatures, turbulence stresses and intensities, mean fluid and solid velocity distributions. There was substantial agreement between the experimental measurements of Tsuji et al. (1987) and the simulation predictions. Particle rotation and interparticle collisions were found to be instrumental in keeping the solid phase suspended in a steady state horizontal flow. The multiphase model of Lun and Liu did not account for the interfacial coupling in kinetic energy.

We follow the approach of Lun and Liu (1997) to study the problem of dilute turbulent gas–solid flows. The turbulent gas phase is modeled by a set of time-averaged conservation equations for mass and momentum, and a second-order multiscale k–ω closure. The solid phase consisting of inelastic, frictional, uniform spherical particles is simulated numerically based on a Lagrangian approach in which the motion of each particle is tracked. A sticking–sliding collision model is employed for the particle–particle collisions and the particle–wall collisions. A two-way coupling numerical iterative scheme is used to incorporate the effects of interfacial interactions in volume fraction, momentum and kinetic energy. The simulation result is compared with the experimental data.

2. Fluid phase transport equations

A set of conservation equations describing the fluid phase of a two-phase fluid–solid mixture may be derived readily by following the traditional control volume approach. The instantaneous conservation of mass, momentum and kinetic energy equations can be expressed as,

$$\frac{\partial}{\partial t}(\epsilon_{\mathrm{f}}\rho_{\mathrm{f}}) + \nabla\cdot(\epsilon_{\mathrm{f}}\rho_{\mathrm{f}}\boldsymbol{u}) = 0 \tag{1}$$

$$\frac{\partial}{\partial t}(\epsilon_{\mathrm{f}}\rho_{\mathrm{f}}\boldsymbol{u}) + \nabla\cdot(\epsilon_{\mathrm{f}}\rho_{\mathrm{f}}\boldsymbol{u}\boldsymbol{u}) = \nabla\cdot(\epsilon_{\mathrm{f}}\boldsymbol{p}_{\mathrm{f}}) + \epsilon_{\mathrm{f}}\rho_{\mathrm{f}}\boldsymbol{g} - \epsilon_{\mathrm{s}}\rho_{\mathrm{s}}\boldsymbol{f} \tag{2}$$

$$\frac{1}{2}\frac{\partial}{\partial t}\left(\epsilon_{\mathrm{f}}\rho_{\mathrm{f}}u^2\right)+\frac{1}{2}\nabla\cdot\left(\epsilon_{\mathrm{f}}\rho_{\mathrm{f}}u^2\boldsymbol{u}\right)=\boldsymbol{u}\cdot\nabla\cdot\left(\epsilon_{\mathrm{f}}\boldsymbol{p}_{\mathrm{f}}\right)+\epsilon_{\mathrm{f}}\rho_{\mathrm{f}}\boldsymbol{g}\cdot\boldsymbol{u}-\epsilon_{\mathrm{s}}\rho_{\mathrm{s}}\boldsymbol{f}\cdot\boldsymbol{u}+\dot{E}_{\mathrm{w}} \tag{3}$$

where $\boldsymbol{f}$ is the local specific resultant interfacial force, and $\boldsymbol{g}$ is the gravitational acceleration. The instantaneous fluid velocity is $\boldsymbol{u}=\boldsymbol{U}+\boldsymbol{u}'$, and the instantaneous fluid stress tensor is $\boldsymbol{p}_{\mathrm{f}}=\boldsymbol{P}_{\mathrm{f}}+\boldsymbol{p}'_{\mathrm{f}}$. Subscripts f and s denote the fluid phase and the solid phase, respectively. Upper case quantities represent time-averaged values, whereas primed quantities depict fluctuation ones. Variables ϵ_{f} and ϵ_{s} are the fluid and solid volume fractions ($\epsilon_{\mathrm{f}}+\epsilon_{\mathrm{s}}=1$), ρ_{f} and ρ_{s} are the fluid and solid mass densities, respectively. The quantity $\dot{E}_{\mathrm{w}}$ in Eq. (3) represents the rate of turbulence kinetic energy generated due to the finite size of the solid particles.

Flows with relatively large and massive particles moving at intermediate particle Reynolds number in the inertia regime are considered in the present study. The solid to fluid mass density ratio, $\rho_{\mathrm{s}}/\rho_{\mathrm{f}}$, is of the order 10^{-3}. The ratio of the particle response time to the eddy turnover time is of the order $>10^2$ (Lun and Liu, 1997). Consequently, the influence of fluid turbulence on the particles' motion would be small. The fluctuations of flow properties of the solid and the fluid phases may be assumed to be uncorrelated. The solid volume fraction, which is a volumetric mean quantity, is assumed to be *independent* of the turbulence averaging time-scale of the fluid phase. After applying the Reynolds time-averaging technique to Eqs. (1)–(3), the following equations for incompressible flows are obtained

$$\frac{\partial}{\partial t}(\epsilon_{\mathrm{f}}\rho_{\mathrm{f}})+\nabla\cdot(\epsilon_{\mathrm{f}}\rho_{\mathrm{f}}\boldsymbol{U})=0 \tag{4}$$

$$\frac{\partial}{\partial t}(\epsilon_{\mathrm{f}}\rho_{\mathrm{f}}\boldsymbol{U})+\nabla\cdot(\epsilon_{\mathrm{f}}\rho_{\mathrm{f}}\boldsymbol{U}\boldsymbol{U})=\nabla\cdot(\epsilon_{\mathrm{f}}\boldsymbol{P}_{\mathrm{f}})+\nabla\cdot(\epsilon_{\mathrm{f}}\tau)+\epsilon_{\mathrm{f}}\rho_{\mathrm{f}}\boldsymbol{g}-\epsilon_{\mathrm{s}}\rho_{\mathrm{s}}\bar{\boldsymbol{f}} \tag{5}$$

$$\frac{\partial}{\partial t}\left(\epsilon_{\mathrm{f}}\rho_{\mathrm{f}}k\right)+\nabla\cdot\left(\epsilon_{\mathrm{f}}\rho_{\mathrm{f}}k\boldsymbol{U}\right)=\epsilon_{\mathrm{f}}\tau:\nabla\boldsymbol{U}-\epsilon_{\mathrm{f}}\nabla\cdot\boldsymbol{q}+\overline{\boldsymbol{u}'\cdot\nabla\cdot\left(\epsilon_{\mathrm{f}}\boldsymbol{p}'_{\mathrm{f}}\right)}-\epsilon_{\mathrm{s}}\rho_{\mathrm{s}}\overline{\boldsymbol{f}'\cdot\boldsymbol{u}'}+\overline{\dot{E}_{\mathrm{w}}} \tag{6}$$

where $\tau=-\rho_{\mathrm{f}}\overline{\boldsymbol{u}'\boldsymbol{u}'}$ is the turbulence stress tensor, $k=\overline{u'^2}/2$ is the specific turbulence kinetic energy, and $\boldsymbol{q}=\rho_{\mathrm{f}}\overline{u'^2\boldsymbol{u}'}/2$ is the turbulence kinetic energy flux. The quantities with overbar represent time-averaged values.

In order to close the above set of equations, we generalize Wilcox's multiscale anisotropic turbulence model for single-phase fluid (Wilcox, 1994) to treat dilute suspensions with solid volume fraction of the order 10^{-3}. After applying time-averaging to equations of higher moment of fluctuation velocities (which are generated using the momentum equation (2)), and after modeling various terms in a manner similar to that performed for a single-phase turbulent fluid, the Reynolds-stress equation for two-phase flows can be written as

$$\frac{\partial}{\partial t}(\epsilon_{\mathrm{f}}\tau_{ij}) + \frac{\partial}{\partial x_k}\left(\epsilon_{\mathrm{f}}U_k\tau_{ij}\right)$$
$$= -\epsilon_{\mathrm{f}}P_{ij} + \frac{2}{3}\beta^*\epsilon_{\mathrm{f}}\rho_{\mathrm{f}}\omega k\delta_{ij} - \epsilon_{\mathrm{f}}\Pi_{ij} + \frac{2}{3}\frac{\partial}{\partial x_k}\left(\epsilon_{\mathrm{f}}\left(\mu + \sigma^*\mu_{\mathrm{T}}\right)\frac{\partial k}{\partial x_k}\delta_{ij}\right) + \epsilon_{\mathrm{s}}\rho_{\mathrm{s}}\left(\overline{u_i'f_j'} + \overline{u_j'f_i'}\right)$$
$$- \frac{2}{3}\overline{\dot{E}_{\mathrm{w}}}\delta_{ij} \tag{7}$$

where μ_{T}, μ and ν are the eddy, absolute and kinematic viscosities, respectively, and δ_{ij} is the unit tensor. The last term on the right hand side of Eq. (7) is included so that contraction of indices in Eq. (7) results in an expression equivalent to Eq. (6). The pressure–strain correlation is

$$\Pi_{ij} = \beta^* C_1\omega\left(\tau_{ij} + \frac{2}{3}\rho_{\mathrm{f}}k\delta_{ij}\right) - \hat{\alpha}\left(P_{ij} - \frac{2}{3}P\delta_{ij}\right) - \hat{\beta}\left(D_{ij} - \frac{2}{3}P\delta_{ij}\right) - \hat{\gamma}\rho_{\mathrm{f}}k\left(S_{ij} - \frac{1}{3}S_{kk}\delta_{ij}\right) \tag{8}$$

where

$$P_{ij} = \tau_{ik}\frac{\partial U_j}{\partial x_k} + \tau_{jk}\frac{\partial U_i}{\partial x_k},$$

$$D_{ij} = \tau_{im}\frac{\partial U_m}{\partial x_j} + \tau_{jm}\frac{\partial U_m}{\partial x_i},$$

and $P = \frac{1}{2}P_{kk}$. The mean strain-rate tensor is $S_{ij} = \frac{1}{2}(\frac{\partial U_i}{\partial x_j} + \frac{\partial U_j}{\partial x_j})$. Similarly, the specific dissipation rate equation (which may be derived from the ε-equation) is

$$\frac{\partial}{\partial t}(\epsilon_{\mathrm{f}}\rho_{\mathrm{f}}\omega) + \frac{\partial}{\partial x_k}(\epsilon_{\mathrm{f}}\rho_{\mathrm{f}}U_k\omega)$$
$$= \alpha\epsilon_{\mathrm{f}}\frac{\omega}{k}\tau_{ij}\frac{\partial u_i}{\partial x_j} - \beta\epsilon_{\mathrm{f}}\rho_{\mathrm{f}}\omega\left(\omega + \hat{\xi}\sqrt{2\Omega_{mn}\Omega_{mn}}\right) + \frac{\partial}{\partial x_k}\left(\epsilon_{\mathrm{f}}(\mu + \sigma\mu_{\mathrm{T}})\frac{\partial\omega}{\partial x_k}\right) + \left(\epsilon_{\mathrm{s}}\rho_{\mathrm{s}}\overline{u_i'f_j'}\right.$$
$$\left. - \overline{\dot{E}_{\mathrm{w}}}\right)\frac{\omega}{k} \tag{9}$$

where the rotation tensor is $\Omega_{ij} = \frac{1}{2}(\frac{\partial U_i}{\partial x_j} - \frac{\partial U_j}{\partial x_i})$. The upper partition energy equation is

$$\frac{\partial}{\partial t}\left(\epsilon_{\mathrm{f}}\rho_{\mathrm{f}}(k-e)\right) + \frac{\partial}{\partial x_k}\left(\epsilon_{\mathrm{f}}\rho_{\mathrm{f}}U_k(k-e)\right) = \epsilon_{\mathrm{f}}\left(1 - \hat{\alpha} - \hat{\beta}\right)P - \beta^*\epsilon_{\mathrm{f}}\rho_{\mathrm{f}}\omega k\left(1 - \frac{e}{k}\right)^{3/2} \tag{10}$$

where e is the kinetic energy of the small eddies, and $k - e$ is the kinetic energy of the large eddies. Since only dilute systems are considered here, the terms,

$$-\nu\overline{u_i'\frac{\partial}{\partial x_k}\left(\epsilon_{\mathrm{f}}\rho_{\mathrm{f}}\frac{\partial u_k'}{\partial x_j}\right)} - \nu\overline{u_j'\frac{\partial}{\partial x_k}\left(\epsilon_{\mathrm{f}}\rho_{\mathrm{f}}\frac{\partial u_k'}{\partial x_i}\right)},$$

in the Reynolds-stress equation (7), and the extra-production/dissipation terms,

$$2\nu\mu\overline{\frac{\partial u_i'}{\partial x_j}\frac{\partial^2}{\partial x_k\partial x_j}\left(\epsilon_{\mathrm{f}}\frac{\partial u_k'}{\partial x_i}\right)}+2\nu\mu\overline{\frac{\partial u_i'}{\partial x_k}\frac{\partial}{\partial x_j}\left(\frac{\partial \epsilon_{\mathrm{f}}}{\partial x_k}\frac{\partial u_i'}{\partial x_j}\right)}-2\frac{\epsilon_{\mathrm{s}}\rho_{\mathrm{s}}\nu}{\beta^* k}\left(\overline{\frac{\partial u_i'}{\partial x_j}\frac{\partial f_j}{\partial x_j}}\right),$$

in the specific dissipation rate equation (9) are basically of higher order, thus they are neglected.

We adopt the low Reynolds number modifications for single-phase fluid given by Wilcox (1994) to the present two-phase multiscale model. The closure coefficients in the above equations are given as follows

$$\alpha^*=\frac{\alpha_o^*+Re_T/R_k}{1+Re_T/R_k}$$

$$\alpha=\frac{4}{5}\frac{\alpha_o+Re_T/R_\omega}{1+Re_T/R_\omega}$$

$$\beta^*=\frac{9}{100}\frac{5/18+\left(Re_T/R_\beta\right)^4}{1+\left(Re_T/R_\beta\right)^4}$$

$$\hat{\gamma}=\frac{1}{4}\frac{\hat{\gamma}_o+Re_T/R_k}{1+Re_T/R_k}$$

$$\hat{\alpha}=\frac{42}{55},\quad \alpha_o=\frac{1}{10},\quad \alpha_o^*=\frac{\beta}{3}$$

$$\beta=\frac{3}{4},\quad \hat{\beta}=\frac{6}{55},\quad \hat{\gamma}_o=\frac{9}{500}$$

$$\sigma^*=\sigma=\frac{1}{2},\quad \hat{\xi}=1$$

$$R_\beta=8,\quad R_k=6,\quad R_\omega=\frac{3}{4}$$

$$C_1=1+4(1-e/k)^{3/2}$$

One fine feature of the multiscale k–ω model is that the equations can be integrated numerically right up to the solid boundaries without the need of damping functions (Wilcox, 1994).

3. Equations of particle motion

Following Lun and Liu (1997), the equation for translational motion of a particle in a turbulent fluid may be written as

$$m_{\mathrm{p}}\frac{\mathrm{d}\mathbf{v}}{\mathrm{d}t} = m_{\mathrm{p}}\mathbf{g} + \mathbf{F}_{\mathrm{D}} + \mathbf{F}_{\mathrm{LS}} + \mathbf{F}_{\mathrm{LM}}. \tag{11}$$

The particle drag force is

$$\mathbf{F}_{\mathrm{D}} = \frac{1}{8}\rho_{\mathrm{f}}\pi d^{2} C_{\mathrm{D}}|\mathbf{v}_{\mathrm{r}}|\mathbf{v}_{\mathrm{r}} \tag{12}$$

where the drag coefficient C_{D} is commonly given as (Clift and Gauvin, 1971)

$$C_{\mathrm{D}} = \frac{24}{Re_{\mathrm{p}}} \quad \left(Re_{\mathrm{p}} < 1\right)$$

$$C_{\mathrm{D}} = \frac{24}{Re_{\mathrm{p}}}\left(1 + 0.15Re_{\mathrm{p}}^{0.687}\right) \quad \left(1 \le Re_{\mathrm{p}} < 1000\right)$$

and $Re_{\mathrm{p}} = \rho_{\mathrm{f}} v_{\mathrm{r}} d/\mu$ is the particle Reynolds number. The Saffman (1965, 1968) lift due to fluid shearing motion is

$$\mathbf{F}_{\mathrm{LS}} = 1.615(\rho_{\mathrm{f}}\mu)^{1/2} d^{2} C_{\mathrm{LS}} \left|\frac{\mathrm{d}U_x}{\mathrm{d}y}\right|^{1/2} (\boldsymbol{u}_x - \mathbf{v}_x). \tag{13}$$

According to Mei (1992), the coefficient C_{LS} may be expressed as

$$C_{\mathrm{LS}} = \left(1 - 0.3314\gamma^{0.5}\right)\exp\left(-0.1Re_{\mathrm{p}}\right) + 0.3314\gamma^{0.5} \quad \left(Re_{\mathrm{p}} \le 40\right)$$

$$C_{\mathrm{LS}} = 0.0524\left(\gamma Re_{\mathrm{p}}\right)^{0.5} \quad \left(Re_{\mathrm{p}} > 40\right)$$

where $\gamma = \left|\frac{\mathrm{d}U_x}{\mathrm{d}y}\right| d/(2v_{\mathrm{r}})$. The Magnus lift due to particle rotation is

$$\mathbf{F}_{\mathrm{LM}} = \frac{1}{2}\rho_{\mathrm{f}} v_{\mathrm{r}}^{2} \frac{\pi d^{2}}{4} C_{\mathrm{LM}} \frac{\omega_{\mathrm{r}} \times \mathbf{v}_{\mathrm{r}}}{|\omega_{\mathrm{r}}||\mathbf{v}_{\mathrm{r}}|}. \tag{14}$$

The Magnus lift coefficient C_{LM} may be expressed as (Lun and Liu, 1997)

$$C_{\mathrm{LM}} = \frac{d|\omega_{\mathrm{r}}|}{|\mathbf{v}_{\mathrm{r}}|} \quad Re_{\mathrm{p}} \le 1)$$

$$C_{\mathrm{LM}} = \frac{d|\omega_{\mathrm{r}}|}{|\mathbf{v}_{\mathrm{r}}|}\left(0.178 + 0.822Re_{\mathrm{p}}^{-0.522}\right) \quad \left(1 < Re_{\mathrm{p}} < 1000\right)$$

In the above equations, m_{p} is the mass of a particle, U_x is the streamwise x-component of the

mean fluid velocity, $\mathbf{v}$ is the instantaneous linear velocity of the particle. The quantities $\mathbf{v}_r = \boldsymbol{u} - \mathbf{v}$ and $\boldsymbol{\omega}_r = \boldsymbol{\Omega}_f - \boldsymbol{\omega}$ are the instantaneous relative linear and angular velocities between the local fluid and the particle, respectively. The local mean angular velocity of the fluid is defined as $\boldsymbol{\Omega}_f = 0.5\nabla \times \boldsymbol{U}$.

Since the density ratio of gas to solid being considered is of the order 10^{-3}, the Basset force due to unsteady history effect and the virtual mass force due to acceleration of fluid surrounding the solid particle are small compared to the drag and the lifts. Thus, they are neglected.

The rate of angular momentum change of a spherical particle interacting with a viscous fluid may be written as (Dennis et al., 1980)

$$\frac{m_p d^2}{10}\frac{d\boldsymbol{\omega}}{dt} = \frac{\rho_f d^2}{64}\left(\frac{6.45}{Re_\omega^{0.5}} + \frac{32.1}{Re_\omega}\right)|\boldsymbol{\omega}_r|\boldsymbol{\omega}_r \quad (20 \le Re_\omega \le 1000)$$

where the spin Reynolds number is defined as $Re_\omega = \rho_f d^2|\boldsymbol{\omega}_r|/(4\mu)$.

4. Collision model

The sticking—sliding collision model presented in Lun and Bent (1994) is employed for particle–particle and particle–wall collisions, in the present study. The model is simple and can reproduce result reasonably close to a number of experimental measurements.

Consider a collision between two inelastic, frictional spherical particles 1 and 2 with velocities $\mathbf{v}_1$ and $\mathbf{v}_2$, angular velocities $\boldsymbol{\omega}_1$ and $\boldsymbol{\omega}_2$, respectively. All collisions are regarded as binary and instantaneous. During the impacts, the interstitial fluid effect is neglected. The peripheral velocities of particles 1 and 2 are

$$\mathbf{g}_1 = \mathbf{v}_1 - \frac{d}{2}(\mathbf{K} \times \boldsymbol{\omega}_1)$$

and

$$\mathbf{g}_2 = \mathbf{v}_2 + \frac{d}{2}(\mathbf{K} \times \boldsymbol{\omega}_2)$$

where $\mathbf{K}$ is the unit vector along the centerline from particle 1 to particle 2. The total relative velocity, $\mathbf{g}_{12}$, at the contact point just prior to the collision is

$$\mathbf{g}_{12} = \mathbf{v}_{12} - \frac{d}{2}(\mathbf{K} \times \boldsymbol{\omega}_{12}) \tag{15}$$

where $\mathbf{v}_{12} = \mathbf{v}_1 - \mathbf{v}_2$ and $\boldsymbol{\omega}_{12} = \boldsymbol{\omega}_1 + \boldsymbol{\omega}_2$. The components of $\mathbf{g}_{12}$ are changed in a collision such that

$$\mathbf{K} \cdot \mathbf{g}_{12}^* = -e_p(\mathbf{K} \cdot \mathbf{g}_{12}) \tag{16}$$

$$\mathbf{K} \times \mathbf{g}_{12}^* = -\beta_p(\mathbf{K} \times \mathbf{g}_{12}) \tag{17}$$

where quantities with superscript asterisk denote post-collisional values, e_p is the coefficient of restitution in the normal direction, and β_p is called the coefficient of restitution in the tangential direction at the point of contact.

Using Eqs. (16) and (17) in Eq. (15), the relationships between the pre- and post-collisional velocities can be written as

$$m_p(\mathbf{v}_1 - \mathbf{v}_1^*) = m_p(\mathbf{v}_2^* - \mathbf{v}_2) = \mathbf{J} \tag{18}$$

$$I(\boldsymbol{\omega}_1^* - \boldsymbol{\omega}_1) = I(\boldsymbol{\omega}_2^* - \boldsymbol{\omega}_2) = -d(\mathbf{K} \times \mathbf{J})/2 \tag{19}$$

and

$$\mathbf{J} = m_p \eta_2 \mathbf{g}_{12} + m_p(\eta_1 - \eta_2)\mathbf{K}(\mathbf{K} \cdot \mathbf{g}_{12}) \tag{20}$$

where $\boldsymbol{J}$ is the impulse, $\eta_1 = (1 + e_p)/2$, $\eta_2 = 0.5(1 + \beta_p)K_r/(1 + K_r)$, and $K_r = 4I/(m_p d^2)$ is a non-dimensional moment of inertia parameter ($K_r = 2/5$ for sphere).

In oblique impacts, the normal and tangential impulses at the contact point are assumed to obey the Coulomb law of friction. In the case of tangential impulse being less than the product of the friction coefficient and the normal impulse, i.e. $|\mathbf{K} \times \mathbf{J}| < \mu_p |\mathbf{K} \cdot \mathbf{J}|$, *sticking contact* occurs. The surface tangential velocity is written as

$$\mathbf{K} \times \mathbf{g}_{12}^* = -\beta_o(\mathbf{K} \times \mathbf{g}_{12}) \tag{21}$$

where β_o is a constant characterizing the restitution of velocity in the tangential direction for sticking contacts, and in general, $0 \le \beta_o \le 1$. Positive β_o denotes particles rebounding with reverse spin caused by the restoration of elastic energy in the tangential direction.

On the other hand, when the tangential impulse is greater or equal to the product of the friction coefficient and the normal impulse, *sliding contact* occurs and the following equality applies,

$$|\mathbf{K} \times \mathbf{J}| = \mu_p |\mathbf{K} \cdot \mathbf{J}|. \tag{22}$$

From Eqs. (20) and (22), the tangential coefficient of restitution is found explicitly as

$$\beta_p = -1 + \mu_p(1 + e_p)(1 + K_r^{-1})|\mathbf{K} \cdot \mathbf{g}_{12}|/|\mathbf{K} \times \mathbf{g}_{12}|. \tag{23}$$

When the collisional properties e_p, β_o and μ_p, and the initial rotational and translational velocities of the particles are known, the impulse $\mathbf{J}$ in Eq. (20), the coefficient β_p in Eq. (21) or (23), and the post-collisional velocities in Eqs. (18) and (19) can be determined.

In the case where a particle collides with a flat wall, the change in particle linear and angular momenta are

$$m_p(\mathbf{v}_1 - \mathbf{v}_1^*) = \mathbf{J} \tag{24}$$

$$I(\boldsymbol{\omega}_1^* - \boldsymbol{\omega}_1) = -d(\boldsymbol{n} \times \mathbf{J})/2 \tag{25}$$

and

$$\mathbf{J} = 2m_{\mathrm{p}}\eta_2\mathbf{g}_{12} + 2m_{\mathrm{p}}(\eta_1 - \eta_2)\boldsymbol{n}(\boldsymbol{n}\cdot\mathbf{g}_{12}), \tag{26}$$

where $\boldsymbol{n}$ is the unit normal perpendicular to the flat wall surface.

5. Tubulence modulation

In the grain-inertia regime, the fluid–solid interaction plays an important role in determining the flow dynamics of the two-phase system. A fairly dilute concentration of solid particles can cause appreciable modification of the fluid phase flow properties. It is obvious in Eq. (5) that the mean specific interfacial force,

$$\bar{\boldsymbol{f}} = \frac{1}{m_p}\sum_{j=1}^{N}\left(\bar{\mathbf{F}}_{\mathrm{D}j} + \bar{\mathbf{F}}_{\mathrm{LS}j} + \bar{\mathbf{F}}_{\mathrm{LM}j}\right), \tag{27}$$

which is the resultant of the drag and lifts acting on the particles, is responsible for the alteration of the mean fluid velocity distribution.

According to Eq. (6), modulation of fluid turbulence kinetic energy can arise from the combined effect of: (i) the mean rate of turbulence kinetic energy dissipation per unit volume due to the interfacial forces, $-\epsilon_{\mathrm{s}}\rho_{\mathrm{s}}\overline{\boldsymbol{f}'\cdot\boldsymbol{u}'}$, and (ii) the mean rate of turbulence kinetic energy production per unit volume due to the finite size of the solid particles, $\dot{E}_w$. Numerical approximation for the interfacial dissipation rate can be obtained readily by using the Lagrangian particle approach, which will be described shortly. Here, we focus on the second term.

Wu and Faeth (1994) measured experimentally the modification of turbulence intensity distributions caused by a single solid sphere in a turbulent flow field inside a pipe. The particle Reynolds number spanned the range 135–1560. The mean streamwise velocity of the turbulent wakes, $U_{\mathrm{w}x}$, was found to scale like self-preserving round laminar wakes with enhanced viscosities due to turbulence. It was given as

$$U_{\mathrm{w}x} = \frac{C_D Re_{\mathrm{t}}}{32}\left(\frac{d}{x - x_o}\right)|\boldsymbol{u} - \mathbf{v}|\exp\left(-\frac{r^2}{2\ell^2}\right) \tag{28}$$

where x is the streamwise distance from the center of the sphere, x_o is the nominal origin of the wake, and r is the radial position. The characteristic wake width is

$$\ell = d\left[2\frac{(x - x_o)}{dRe_{\mathrm{t}}}\right]^{1/2}$$

The turbulence Reynolds number is

$$Re_{\mathrm{t}} = \frac{d|\boldsymbol{u} - \mathbf{v}|}{\nu_{\mathrm{t}}}$$

The local turbulence kinematic viscosity may be expressed as

$$\nu_t/\nu = 1 \quad 0 \le Re_p \le Re_c$$

$$\nu_t/\nu = 1 + 1.295\left(\frac{Re_p - Re_c}{135 - Re_c}\right) \quad Re_c < Re_p < 135$$

$$\nu_t/\nu = 0.017 Re_p \quad 135 \le Re_p < 310$$

$$\nu_t/\nu = 1.2 + 0.000042 Re_p^2 \quad 310 \le Re_p < 610$$

$$\nu_t/\nu = 0.029 Re_p \quad 610 \le Re_p < 1560 \tag{29}$$

The first two correlations in Eq. (29) are proposed here to complement the rest given by Wu and Faeth (1994), in order to extend the particle Reynolds number to a lower range of values. The first relationship is rather obvious. In the second one, the viscosity ratio is assumed to vary linearly with Re_p similar to the rest, except the transitional one for $310 \le Re_p < 610$. The onset of flow separation around a smooth sphere in a laminar environment occurs at a critical particle Reynolds number Re_c of 24 (Taneda, 1956). Such a critical value is likely to be lowered in cases with turbulent surroundings. In addition, particle rotation and the finite size effect of neighboring particles could alter the critical Reynolds number as well. The neighboring particle-size effect is especially prominent in high particle concentrations. Unfortunately, due to the lack of pertinent information, the choice of Re_c is somewhat arbitrary at the present time. We have chosen Re_c so as to "optimize" the agreement between the simulation predictions and the experimental result.

In the range of $135 \le Re_p < 1560$ (Wu and Faeth, 1994), the dimensionless *streamwise* r.m.s. velocity fluctuations in the near wake region, $\sqrt{\overline{u'^2_{wx}}}/\sqrt{\overline{u'^2_x}}$, was found to be 4 to 6; where $\sqrt{\overline{u'^2_x}}$ is the ambient turbulence intensity along the axis of the wake. In the range of $135 \le Re_p \le 240$, the turbulence modification due to the *cross-stream* r.m.s. velocity fluctuations, $\sqrt{\overline{u'^2_{wr}}}/\sqrt{\overline{u'^2_r}}$, was relatively small. However, when the particle Reynolds number increased to the range of $300 \le Re_p \le 600$, the dimensionless cross-stream ratio also became 4 to 6. The cross-stream r.m.s. velocity fluctuations was mainly caused by the shedding of vortices behind the sphere, once the critical Strouhal number at Re_p of 300 was surpassed. For $Re_p > 600$, the dimensionless cross-stream ratio increased somewhat further.

On the basis of the above observation, we propose here a model to estimate the modulation of turbulence due to solid particles for $0 \le Re_p \le 1560$. The present flow system is rather complex since each solid particle can traverse freely in three-dimension unlike the axisymmetric case tested by Wu and Faeth. First, we assume that the wake r.m.s. velocity fluctuation, $\sqrt{\overline{u_w^2}}$, varies exponentially in the axial and radial directions similar to U_{wx} in Eq. (28). Furthermore, it is proportional to the local *ambient* r.m.s. velocity fluctuation $\sqrt{\overline{u'^2}}$ $(= \sqrt{2k})$, thus,

$$\sqrt{\overline{u'^2_{\rm w}}} = \sqrt{2kC_{\rm W}}\exp\left(-\frac{r^2}{2\ell^2}\right) \tag{30}$$

Inferring from the experimental result of Wu and Faeth, the wake coefficient $C_{\rm W}$ may be expressed as

$$C_{\rm W} = 0 \quad \left(Re_{\rm p} \le Re_{\rm c}\right)$$

$$C_{\rm W} = 16/3 \quad \left(Re_{\rm c} < Re_{\rm p} < 310\right)$$

$$C_{\rm W} = 34/3 \quad \left(310 \le Re_{\rm p} \le 1560\right) \tag{31}$$

The first relation in Eq. (31) states that if $Re_{\rm p}$ is less than $Re_{\rm c}$, then the particle causes no turbulence modulation. For $Re_{\rm c} < Re_{\rm p} < 310$, only the "streamwise" component is effective in augmenting the turbulence fluctuations. By employing a constant ratio of $\sqrt{\overline{u'^2_{{\rm w}x}}}/\sqrt{\overline{u'^2_x}} = 4$, and approximating $\overline{u'^2_x}$ to be $2k/3$, we obtain the factor 16/3 in the second expression. In the third one, according to the measurements in the pipe-flow experiment of Wu and Faeth, the "cross-stream" to "streamwise" r.m.s. wake velocity fluctuation ratio, $\sqrt{\overline{u'^2_{\rm wr}}}/\sqrt{\overline{u'^2_{{\rm w}x}}}$, is 3/4. Assuming that the second cross-stream ratio, $\sqrt{\overline{u'^2_{{\rm w}\theta}}}/\sqrt{\overline{u'^2_{{\rm w}x}}}$, is of the same order of magnitude as the first, one obtains $C_{\rm W} = 34/3$. The turbulence modulation imparted in the fluid phase by the solid phase is assumed to decay in the same manner as the regular eddies, since the wakes are carried downstream by the surrounding fluid.

Our main interest is to approximate the rate of turbulence kinetic energy per unit volume, $\dot{E}_{\rm w}$, which is generated by the wakes behind the solid particles. The effect of particle rotation on the wake intensity is assumed to be negligibly small. One may estimate the rate of turbulence kinetic energy generated *per solid particle* by using

$$\dot{e}_{\rm w} = \oint_{cs} \frac{\rho_{\rm f}}{2}\overline{u'^2_{\rm w}}\mathbf{v}_{\rm r}\cdot\boldsymbol{n}\,{\rm d}A.$$

where $\boldsymbol{n}$ is the unit normal of the small area ${\rm d}A$. After substituting Eq. (30) into the above integral, and integrating over the entire area from radius $r = 0$ to ∞ at $(x - x_o)/d = 1$, one obtains

$$\dot{e}_{\rm w} = 2\pi C_{\rm W}\rho_{\rm f}\nu_{\rm t}k$$

Note that since $\dot{e}_{\rm w}$ is a local quantity for each particle per se, the local interfacial relative velocity ($\mathbf{v}_{\rm r}$) and the specific kinetic energy (k) are treated as constants in the integration. Finally, we have $\dot{E}_{\rm w} = n\dot{e}_{\rm w}$, i.e.

$$\dot{E}_{\rm w} = 2\pi n C_{\rm W}\rho_{\rm f}\nu_{\rm t}k \tag{32}$$

where n is the solid particle number density (i.e., number of particles per unit volume). With

Eqs. (29) and (32), it is now possible to assess the degree of turbulence modulation due to solid particles at Re_p up to 1560.

Other researchers had previously modeled the turbulence kinetic energy production rate; for example Yuan and Michaelides (1992) and Yarin and Hetsroni (1994). Yuan and Michaelides proposed that $\dot{E}_w$ depended on the fluid mass density, the kinetic energy difference between the fluid and the solid particle, the square of the base diameter of a half ellipsoidal wake, and a certain unknown function of the effective length of the wake. By using a boundary layer approximation and assuming a quasi-stationary character of the wake with a certain velocity profile, Yarin and Hetsroni obtained an expression for $\dot{E}_w$, which was found to be a function of the fluid–solid particle relative velocity, the "mass content" of a particle in a fluid element, the interfacial mass density ratio, and the drag coefficient. Similar to the present work, the empirical coefficients in both models must be determined by means of experiments.

6. Numerical procedure

The above turbulent two-phase model is applied to simulate gas–solid mixture flows in vertical pipes in an approach similar to that taken by Lun and Liu (1997) for flows in horizontal channels. A central difference scheme with second order accuracy is used to numerically integrate the fluid-phase mean transport equations (4), (5) and (7)–(12). The instantaneous fluid velocity, which is needed in the integration of the particle motion equations in the solid-phase computation, is composed of the sum of a mean component and a fluctuation component. The *mean* fluid velocity field is obtained from the finite difference method, whereas the fluid *fluctuation* velocity at each node is sampled from a Gaussian distribution based on the r.m.s. of the turbulence intensity in each direction. The mean and instantaneous fluid properties at the particle center are linearly interpolated from values at the closest grid nodes of the fluid finite-difference scheme enclosing the particle.

Each fluctuation velocity represents an energetic eddy with a certain lifetime interacting with the solid particles in its vicinity. The eddy lifetime is randomly sampled from a Gaussian distribution based upon the random lifetime of turbulent eddies with the Lagrangian integral timescale. For dilute fluid–solid systems, the eddy lifetime given by Wilcox's multiscale model for single fluid-phase may be adopted (Wilcox, 1994),

$$T_L = 0.09\frac{k}{\varepsilon}$$

where $\varepsilon = \nu\overline{\frac{\partial u_i'}{\partial x_j}\frac{\partial u_i'}{\partial x_j}}$ is the specific energy dissipation rate and is related to the specific dissipation rate ω as $\varepsilon = \beta^*\omega k$.

The mean interfacial momentum flux per unit volume term, $\epsilon_s\rho_s\bar{\boldsymbol{f}}$, in Eq. (27) for a particular computational cell can be determined simply by time-averaging the net rate of momentum change of particles passing through the cell within a certain duration. Likewise, the mean rate of turbulence kinetic energy dissipation per unit volume due to interfacial forces ($-\epsilon_s\rho_s\overline{u_i'f_j'}$) in Eq. (7) can be obtained promptly since the fluctuation fluid velocity associated with each particle is made available as described earlier. The mean rate of turbulence kinetic energy production per unit volume, $\dot{E}_w$, can be computed by time-averaging expression (32).

In a number of preliminary simulations of vertical pipe-flows, we find that the diagonal components of $-\epsilon_s\rho_s\overline{u_i'f_j'}$ are the dominant contributions, whereas the off-diagonal ones are typically two order of magnitude smaller. Consequently, the off-diagonal components are neglected in the computations presented herein.

Initially, solid particles are randomly distributed inside a control volume enclosed by a cylindrical solid side-wall and top and bottom periodic walls. Random fluctuation velocities in addition to a mean velocity are assigned to each particle.

The motions of the particles are assumed to be uncorrelated and there is no other particle–particle interaction except direct hard collisions. By numerically integrating the coupled translational and rotational equations of motion for each particle in a small time step Δt using fourth-order Runge–Kutta, a particle can be advanced from one position to another. Since the non-dimensional time Δt^* $(= \Delta t/(d/U_m))$ is typically taken to be of the order 0.01, the numerical integration error of the Runge–Kutta scheme is of the order 1.0E−10. The particles are moved at small time increment so that they traverse no more than 20% of the particle diameter in each step. This ensures that the particles will not unknowingly pass through each other or the solid wall and the probability of simultaneous multiple collisions is eliminated. After all the particles had been moved, the distances between particle centers and between particles and solid walls are computed. If the distance between two particle centers is less than a particle diameter, then a particle–particle collision had occurred within the last time step. Each collided particle is moved back to its old position at Δt, and then to the location where it just touches its colliding partner. The impulse and the post-collisional particle velocities are calculated according to Eqs. (18)–(20). A new trajectory for the collided particle is computed. If however no collision has occurred at all, or after all the collisions have been dealt with, then every particle is moved again for another Δt. After a specific time, new fluid properties are computed by incorporating into the fluid finite-difference calculation, the information obtained from the solid-phase computation; namely, the mean solid volume fraction, the mean interfacial momentum flux per unit volume, and the mean interfacial turbulence kinetic energy dissipation and production rates associated with each grid cell. The new mean fluid properties will subsequently be used in the solid-phase computation. Such a two-way coupling iterative procedure continues until a specific time for ending the computation is reached. One way to determine whether the simulation of the solid-phase flow has reached steady state is that the stepwise dimensionless error bounds for the total particle kinetic energy and the particle bulk velocity approaches zero; a typical value of 0.01 is used for both, in the present study. Similarly, a convergence error bound of the order 0.01 for the bulk velocity is set for the integration of the fluid phase flow. In other words, the overall accuracy of the numerical scheme is of second order.

7. Result

The present turbulent two-phase model is implemented to simulate the experiments of air–solid flow in a vertical pipe conducted by Tsuji et al. (1984). The pipe inner diameter (D) was 30.5 mm. Polystyrene beads were transported in the system. Unfortunately, the material properties of the solid particles and the pipe are not available. The particle–particle and

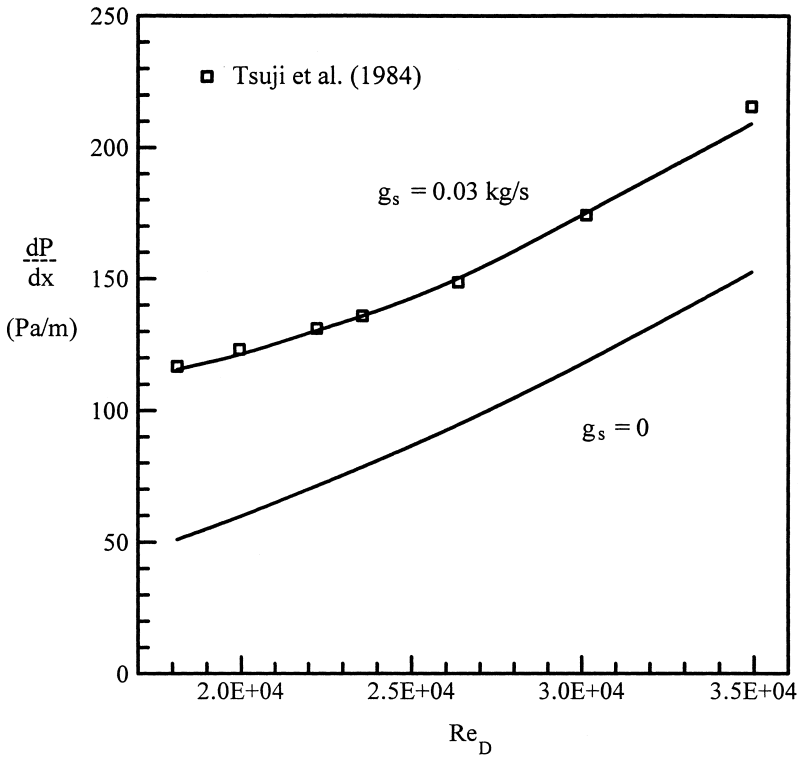

Fig. 1. Variation of pressure gradient with pipe Reynolds number for constant solids mass flow rate, g_s (curves are predictions).

particle–wall collisional properties (e_p, β_o and μ_p) are regarded as same. The values of $e_p = 0.9$, $\beta_o = 0.4$, $\mu_p = 0.47$ (Lun and Liu, 1997), and the critical particle Reynolds number of $Re_c = 18$ are used in the present computations. All plots in the paper are dimensionless, unless otherwise specified.

Fig. 1 shows the variation of pressure gradient with increasing carrier fluid velocity expressed in terms of the pipe Reynolds number, $Re_D = U_m D/\nu$; where U_m is the bulk fluid velocity. The mass flow rate of 0.5 mm particles is kept constant at $g_s = 0.03$ kg/s. Excellent agreement is found between the simulation result and the experimental measurements. The predictions for single-phase fluid flows are also plotted in the figure. The difference in pressure gradient between the suspension and the single-phase fluid flow represents the additional pressure loss in transporting the solid phase, and it is clearly significant. For example, the difference increases from a factor of 4/3 to 2 with increasing mass loading (m_L) from 2 to 3.8. In these dilute systems, the kinetic mode dominates over the collisional mode in the solid phase, thus the collisional properties of the solid particles and the pipe have little influence on the pressure drop.

Distributions of mean fluid velocity ($U_x^* = U_x/U_m$) and streamwise turbulence intensity ($u_x^* = (\overline{u'^2_x})^{1/2}/U_m$) for fixed Re_D are plotted in Figs. 2–4 for different sizes of particles. Unfortunately, the bulk fluid velocity of the experiments are not available. The mean fluid

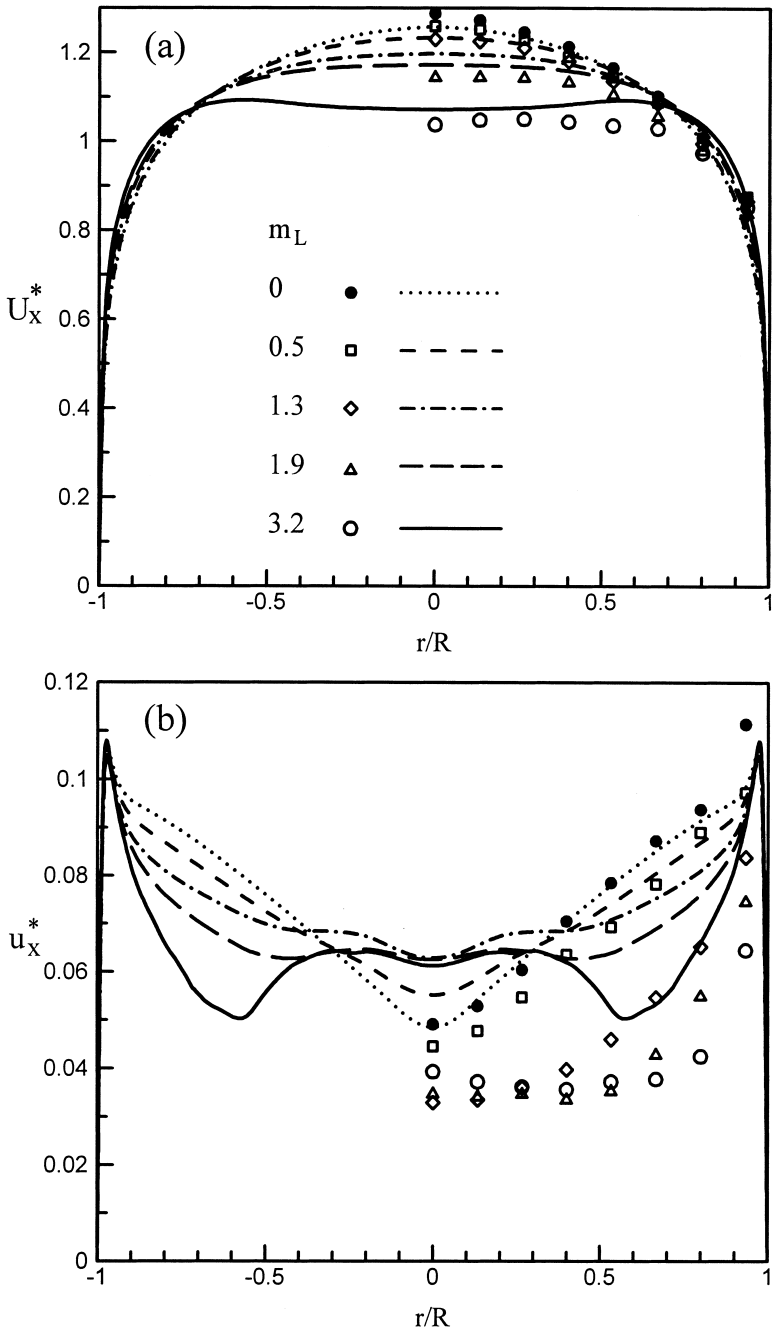

Fig. 2. (a) Mean fluid velocity distributions and (b) streamwise turbulence intensity profiles in flows with 0.2 mm particles. Symbols: Tsuji et al. (1984); curves are predictions for $U_m = 10.6$ m/s.

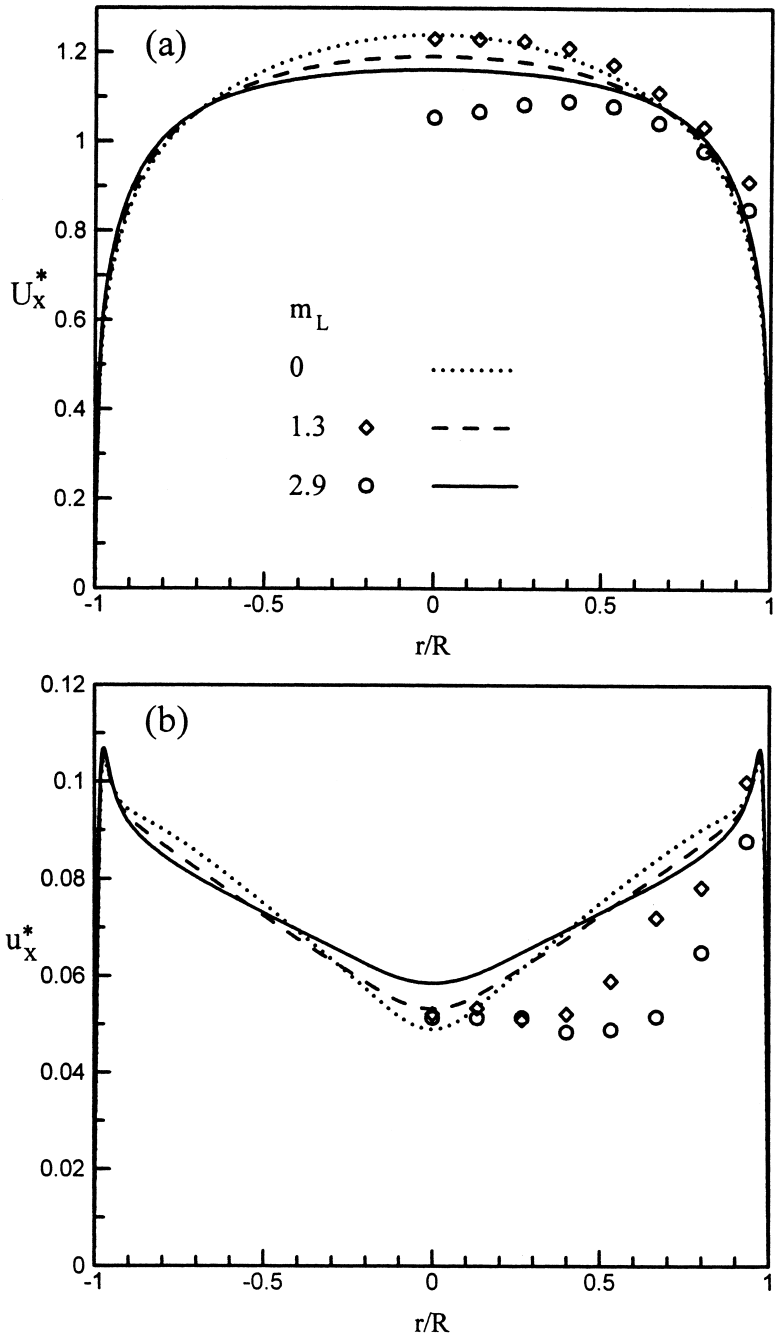

Fig. 3. (a) Mean fluid velocity distributions and (b) streamwise turbulence intensity profiles in flows with 0.5 mm particles. Symbols: Tsuji et al., 1984; curves are predictions for $U_m = 10.8$ m/s.

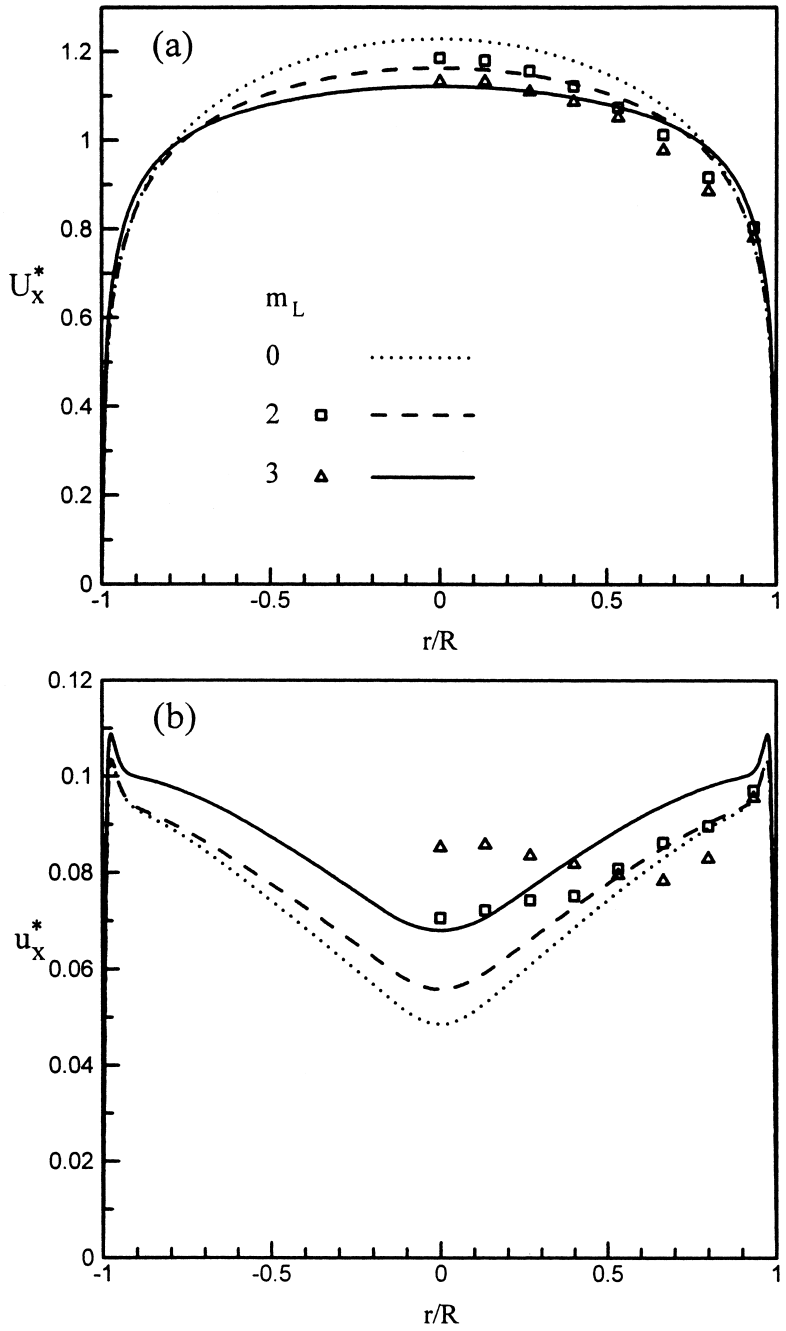

Fig. 4. (a) Mean fluid velocity distributions and (b) streamwise turbulence intensity profiles in flows with 1 mm particles. Symbols: Tsuji et al., 1984; curves are predictions for $U_m = 11.3$ m/s.

velocities and turbulence intensities are normalized by the constant bulk fluid velocity used in the simulations. The variable r is nondimensionalized by the pipe radius, R. There is reasonable qualitative agreement between the simulation predictions and the experimental measurements. Somewhat better quantitative agreement between the two can be obtained if the "actual" bulk fluid velocity for each test run is used. Nonetheless, we may estimate U_m in these *dilute* flows by using trapezoidal quadratures and assuming uniform solid concentration distributions. As a result, we find that the bulk fluid velocities differ to some degree in most experiments. For example, in the case of 0.2 mm particles shown in Fig. 2, the U_m are approximately 10.95, 10.85, 10.48 and 10.14 m/s for mass loading of 0.5, 1.3, 1.9 and 3.2, respectively. Similarly, U_m for cases of 0.5 mm particles are about 10.7 and 10.8 m/s for mass loading of 1.3 and 2.9, whereas those of 1 mm particles are about 11.0 and 11.7 m/s for mass loading of 2 and 3, respectively. In fact, the differences in U_m show up in the figures when one compares the normalized velocity profiles in each set of experiments. The simulations are based on a constant U_m (e.g. 10.6 m/s or $Re_D = 21600$, in Fig. 2). Owing to continuity in incompressible flow, a decrease in mean fluid velocity near the center region always accompanies an increase in the outer region of the profile. As a result, crossovers of mean velocity profiles appear. The majority of the experimental velocity profiles do not cross each other. The centerline fluid velocity is very sensitive to the bulk fluid velocity, the mass loading, and whether the flow has fully developed or not. Thus, it is not the most appropriate quantity to be used for nondimensionalizing flow properties such as velocities and turbulence intensities. The quantitative discrepancies between the predictions and the measurements are partly due to the differences in U_m. Another factor possibly responsible for the discrepancies in turbulence intensities is that the laser Doppler velocimeter (LDV) used by Tsuji et al. is not a 100% non-intrusive measurement technique. The fluid phase was seeded with fine tracer particles so that signals from particles passing over the laser beams could be correlated to yield quantities such as fluid velocities and turbulence intensities. The mean diameter of the ammonium chloride smoke particles used by Tsuji et al. was 0.6 μm. Such fine particles clang to the pipe wall. The test section was cleaned about every 20 min in each test. The smoke particles not only changed the surface properties of both the pipe and the solid particles, but they could attenuate the turbulence intensities as well. Unfortunately at the present time, it is difficult to estimate the extent of the influences of the smoke particles in the measurements.

It is instructive to examine the effects of various terms in the turbulence kinetic energy equation (6), particularly the mean rate of turbulence kinetic energy dissipation per unit volume due to interfacial forces, $\gamma_f = -\epsilon_s \rho_s \overline{\boldsymbol{f}' \cdot \boldsymbol{u}'}$, and the mean rate of turbulence kinetic energy production per unit volume due to the finite size of solid particles, $\dot{E}_w$. As it turns out, the extra dissipation term, $\gamma_f^* = \gamma_f/(\rho_f U_m^4/\nu)$ is a destabilizing term, and without the production term, $\dot{E}_w^* = \dot{E}_w/(\rho_f U_m^4/\nu)$, the numerical solution diverges. Fig. 5 presents the simulation result for cases with and without the two terms in the energy equation (6) (and correspondingly in the dissipation equation (9)). The result for the single-phase fluid flow is also plotted in the figure. Computation having the two energy terms (solid curves) shows that the mean fluid velocity becomes flatter than the one without (dotted curves in Fig. 5(a)), even though the streamwise resultant interfacial force, $\bar{f}_x^* = \bar{f}_x/(U_m^3/\nu)$, (see Fig. 5(b)) is slightly smaller. This illustrates that the turbulence kinetic energy, $k^* = k/U_m^2$ (Fig. 5(c)) can indeed influence the

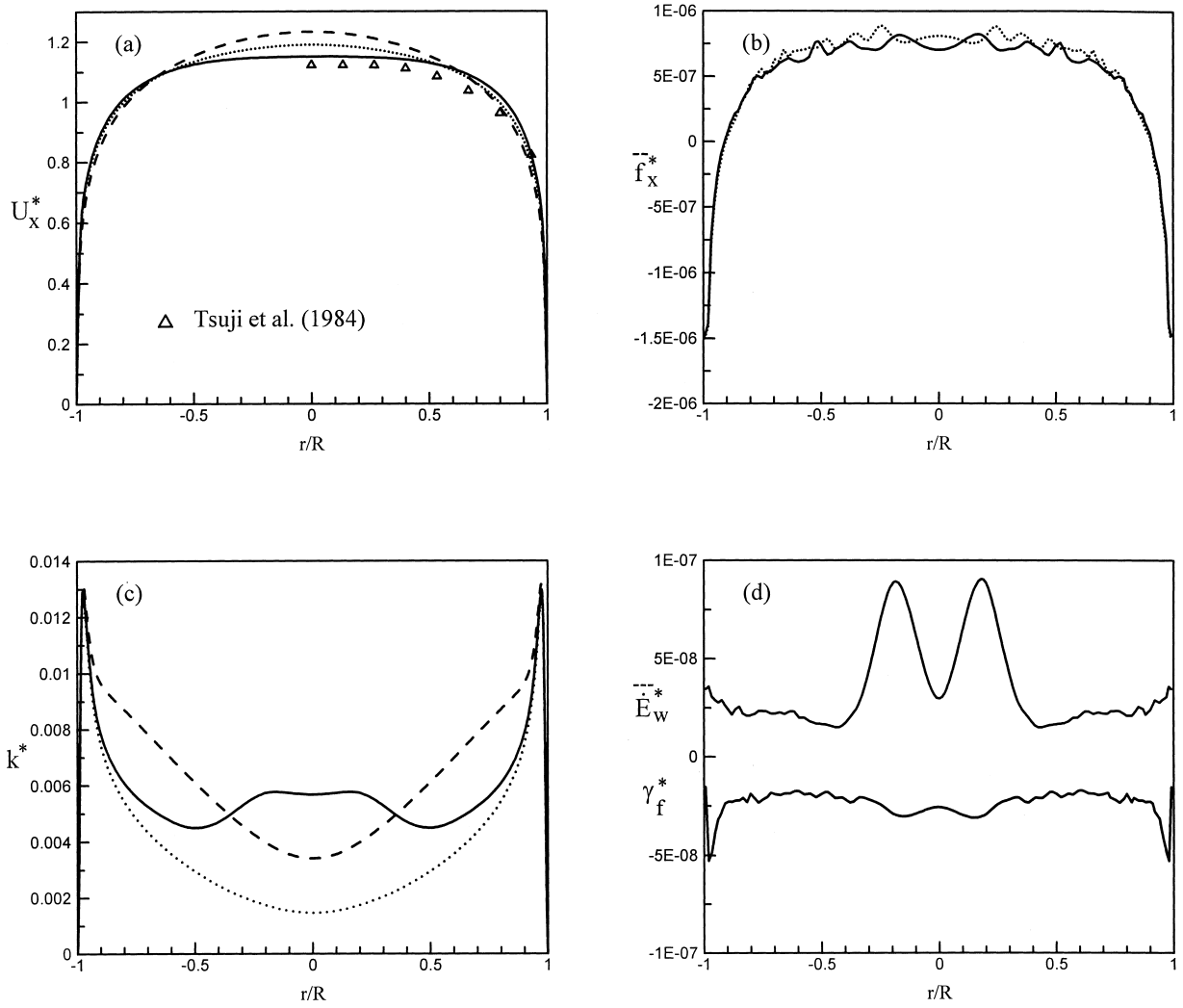

Fig. 5. Distributions of: (a) mean fluid velocity, (b) streamwise resultant interfacial forces, (c) turbulence kinetic energy, and (d) mean rates of extra dissipation and production for system with 0.2 mm particles, $m_L = 1.9$, and $U_m = 10.6$ m/s. Dashed curves: single-phase fluid flow; dotted curves: two-phase flow simulation without the extra dissipation and production terms; solid curves: simulation with both terms.

mean fluid velocity significantly through the turbulence stress terms in the momentum equation.

In the absence of both the mean rates of extra dissipation and production terms (Fig. 5(d)), the numerical solution (dotted curve) shows that there exists inherent turbulence damping in the suspension as shown in Fig. 5(c). Such an inherent damping of turbulence intensities arises due to the alteration of the mean fluid velocity distribution incurred by the mean interfacial force. The inherent turbulence damping can be best realized perhaps in the suspension of small and light particles. The turbulent fluid essentially drives and controls the motions of the solid

particles. The mean particle Reynolds number Re_p is smaller than the critical particle Reynolds number Re_c for flow separation, hence, there would be very limited turbulence enhancement. As a result, small and light particles would cause turbulence attenuation in most situations. As the particle diameter increases, Re_p can become larger than Re_c. Consequently, the turbulence production term, $\dot{E}_w$, can overcome the inherent damping as well as the extra dissipation (γ_f) in certain region of the flow field. Thus, the final outcome would be a combination of turbulence damping in one area and augmentation in another. In the case of vertical pipe-flow shown in Figs. 2(b) and 3(b), turbulence enhancement occurs in the center region while turbulence damping takes place in the outer region. For large particles, if the range of Re_p is greater than 300, the turbulence field is always intensified by the vortex shedding of the solid phase (Fig. 4(b)). This is consistent with experimental result (Hetsroni, 1989). It is noteworthy that the overall mean Re_p for the 0.2 mm particles is of the order of 20; 85 for 0.5 mm particles, and 350 for 1 mm particles.

Fig. 6(a) and (b) present the distributions of velocities for systems of 0.2 and 0.5 mm polystyrene particles (Tsuji et al., 1984), respectively, while Fig. 6(c) and (d) show those for 0.2 and 0.4 mm glass beads (Lee and Durst, 1982). Fortunately, for this particular set of polystyrene bead experiments, Tsuji et al. provided the bulk fluid velocities in addition to the centerline ones. Thus, the measured bulk fluid velocities are used as the normalization parameters. The values of $e_p = 0.97$, $\beta_o = 0.44$, $\mu_p = 0.40$ (Lun and Liu, 1997), and $Re_c = 18$ are used in the present simulations of air–glass particle flow. However, since Lee and Durst specified only the centerline air velocities (U_c), the quantities plotted in Fig. 6(c) and (d) are normalized by U_c. In general, the simulation predictions and the velocity measurements agree reasonably well. We have shown only half of the symmetric velocity profile of the solid phase in Fig. 6 in order to avoid confusion with those of the fluid phase. It is easy to locate the change of sign in the mean relative velocities between the two phases as computed in the simulation. For example, in the case of 0.2 mm polystyrene particles (Fig. 6(a)), the distance of the sign change occurs at about 0.1 R from the wall.

Lee and Durst (1982) also reported the r.m.s fluctuation velocities of the fluid and solid phases in addition to the velocity profiles for 0.8 mm glass particles. However, when the present multiphase model is applied to simulate such a case, the solid particles are found to be continuously falling down instead of being lifted up. When the experimental value of maximum interfacial relative velocity at the centerline of the flow is used to calculate the drag force acting on a 0.8 mm glass particle, the ratio of the drag to particle weight turns out to be about 0.6. As one examines the same ratio for all the other flow systems presented in this paper, the values vary somewhat but are always greater than unity as one may expect in these dilute systems. Thus, perhaps such an anomaly was caused by a wide distribution of sizes in the particular assortment of glass beads used by Lee and Durst.

Maeda et al. (1980) used relatively small copper particles with 0.093 mm diameter, and glass particles with 0.045 and 0.136 mm diameters in their vertical pipe-flow experiments. When the present simulation is used to predict the flow properties of these experiments, the extra turbulence production rate $\dot{E}_w$ in Eq. (6) turns out to be smaller than the extra dissipation rate γ_f in the centerline region by a fair amount, as a result, it leads to divergence in the computation of the fluid phase. The particle Reynolds number in these experiments is around

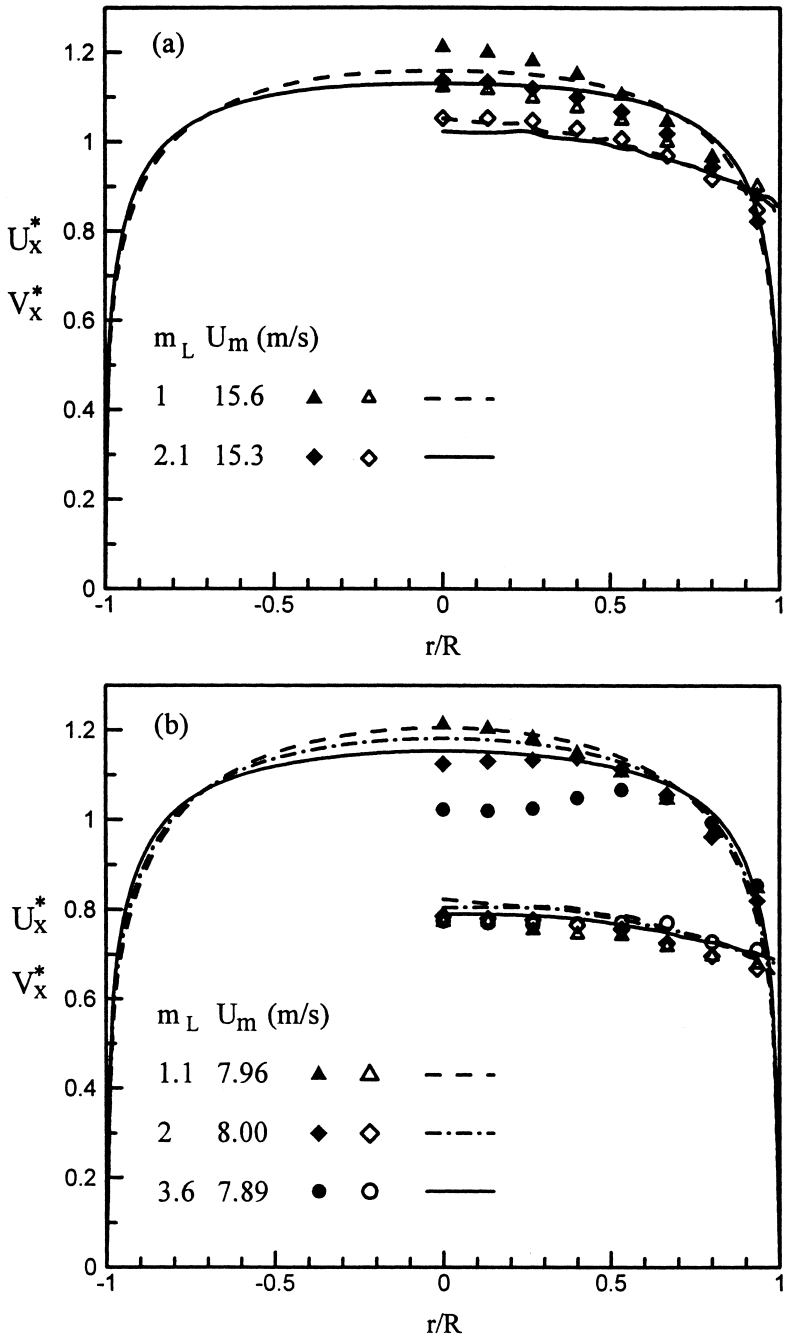

Fig. 6. Distributions of mean fluid velocity (solid symbols) and solid particle velocity (open symbols) for systems with: (a) 0.2 mm, (b) 0.5 mm diameter polystyrene beads (Tsuji et al., 1984), (c) 0.2 mm, and (d) 0.4 mm diameter glass beads (Lee and Durst, 1982). Curves are predictions.

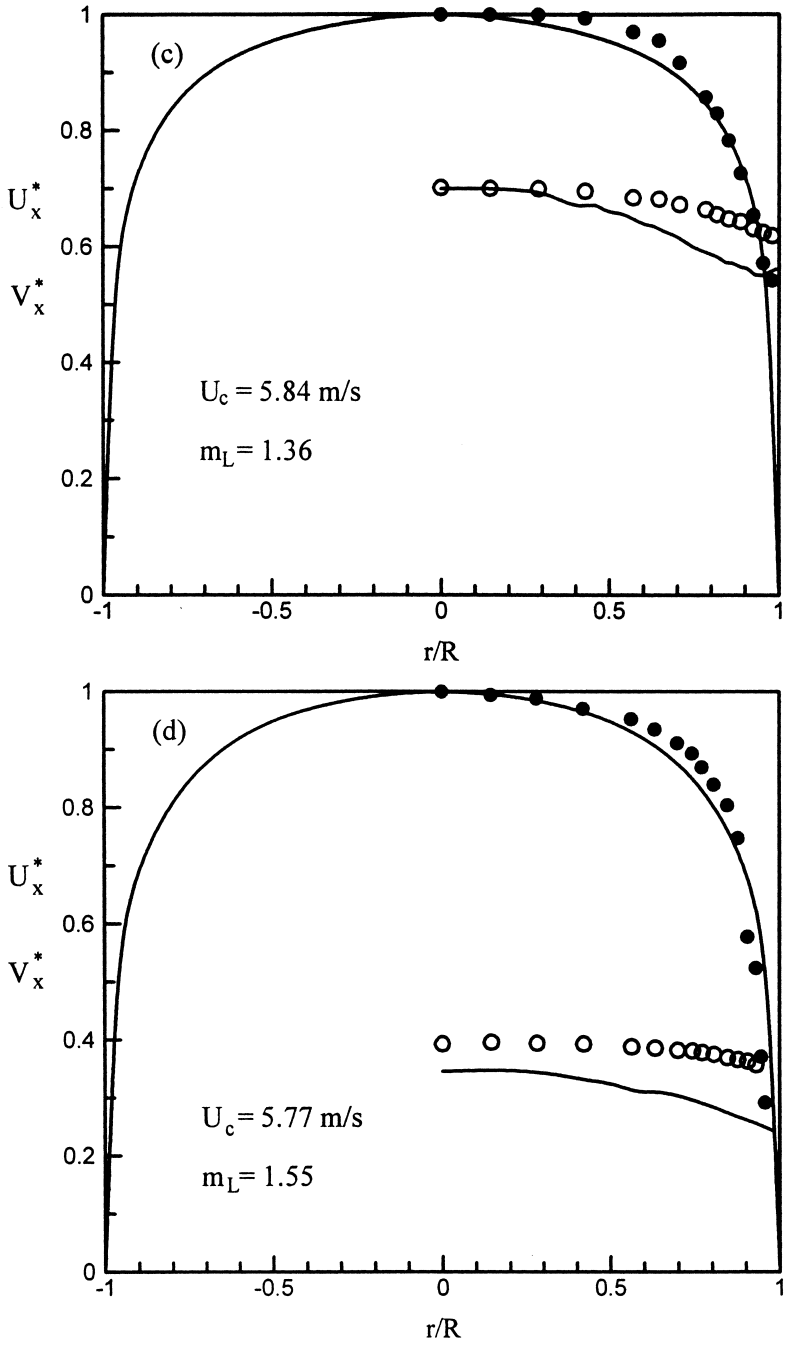

Fig. 6 (*continued*)

10, in which case, effects such as crossing trajectory and fluid–solid fluctuation correlation can become important. Further study of these low particle Reynolds number flows is necessary.

Simulation results for macroscopic properties such as solid concentration, resultant interfacial force, turbulence intensity, rates of extra dissipation and production of kinetic energy, mean particle rotational speed, translational and rotational granular temperatures, fluid and solid stresses are shown in Figs. 7–11. The majority of these flow properties is rather difficult to obtain in physical experiments, and therefore have not been reported. The plots are

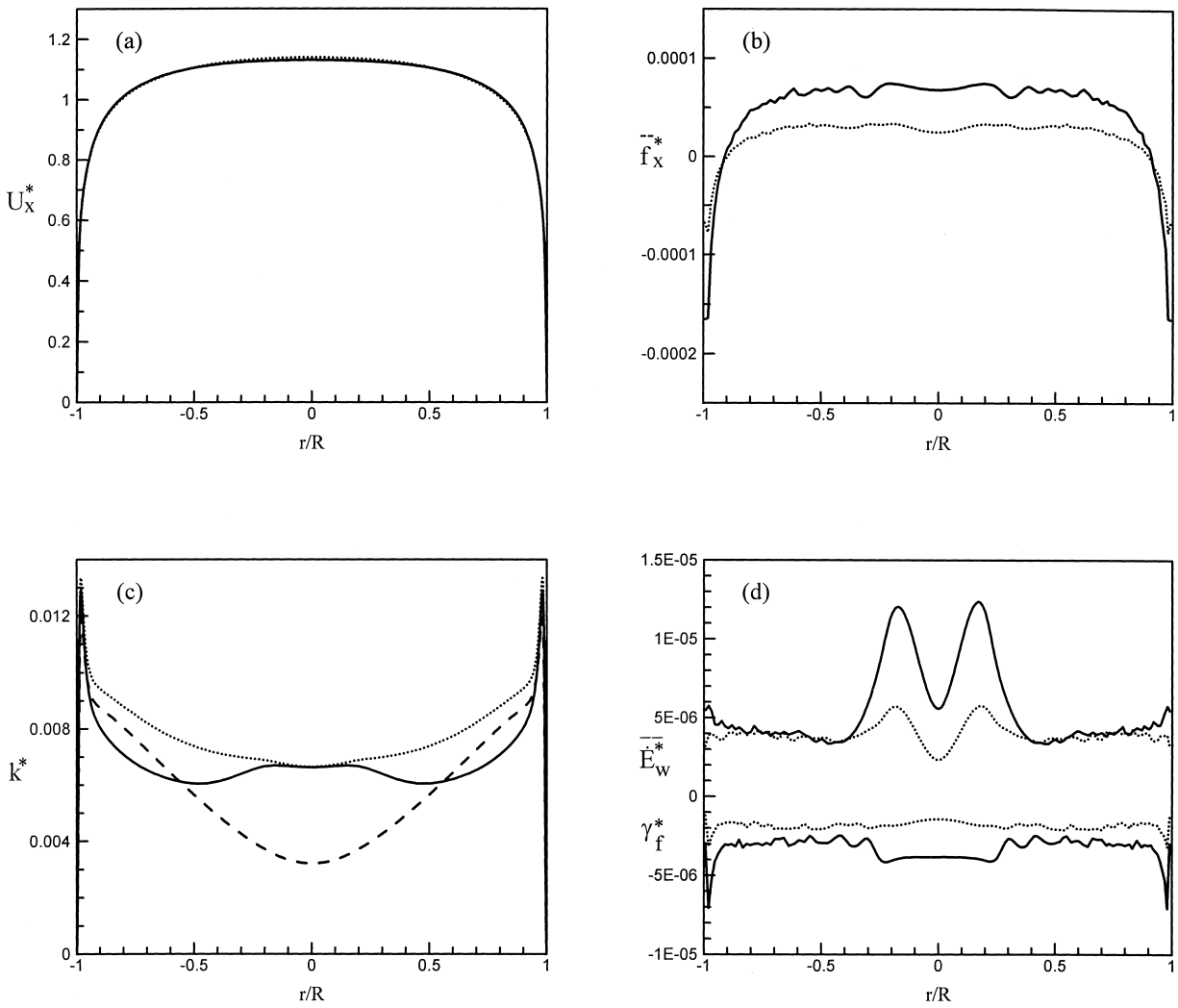

Fig. 7. Distributions of: (a) mean fluid velocity, (b) streamwise resultant interfacial forces, (c) turbulence kinetic energy, and (d) mean rates of extra energy dissipation and production. Dashed curves: $m_L = 0$; dotted curves: $m_L = 1$; solid curves: $m_L = 2.1$.

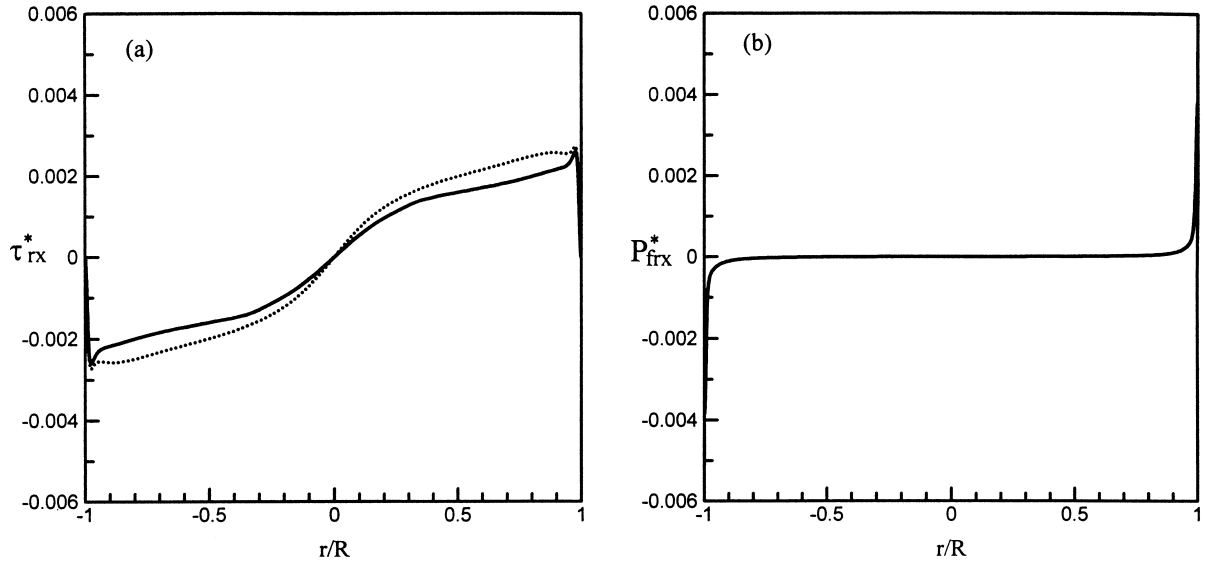

Fig. 8. (a) Reynolds shear stress, (b) molecular shear stress.

based on simulated flows with 0.2 mm particles, $U_m = 15.3$ m/s, and mass loading of 1 and 2.1. In the figures, dotted curves and solid curves represent cases of $m_L = 1$ and 2.1, respectively.

The mean fluid velocity profile is modestly flattened as the mass loading increases from 1 to 2.1, as shown in Fig. 7(a). As one might anticipate, the mean streamwise interfacial force increases with increasing mass loading except in the near wall region (Fig. 7(b)). Near the side-

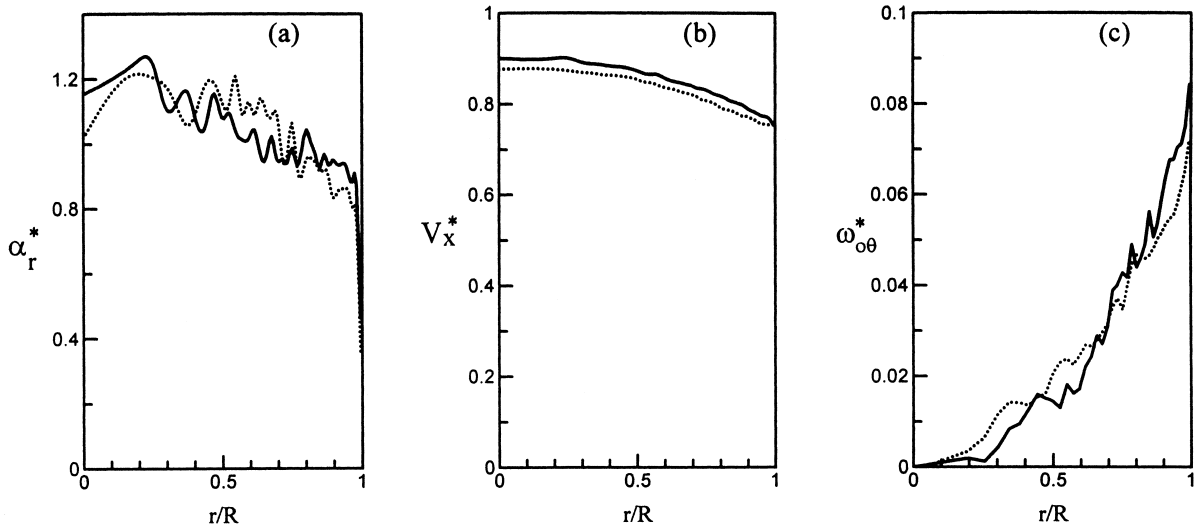

Fig. 9. Distributions of: (a) solid concentration, (b) mean particle linear velocity, and (c) mean particle angular velocity.

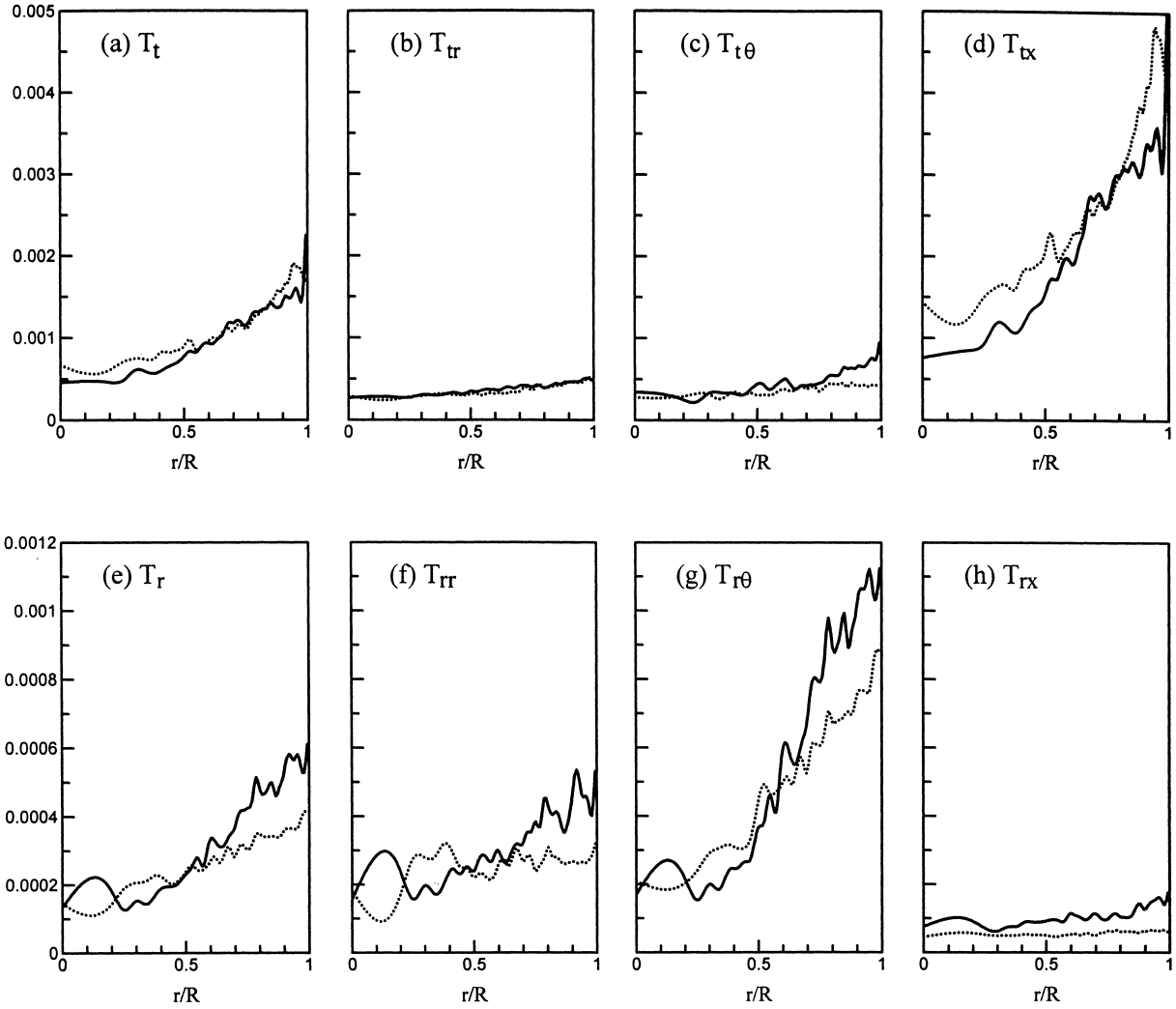

Fig. 10. Distributions of granular translational and rotational temperatures.

wall, since the solid particles often travel faster than the fluid, the relative interfacial velocity becomes negative and so does the interfacial force. In fact, the points at which the profiles intersect the abscissa are the same locations at which the mean velocity profiles of the fluid and the solid phase cross each other (see Fig. 6(a)). The mean interfacial force at the wall is about twice that near the center region as shown in Fig. 7(b).

For the relatively small 0.2 mm polystyrene particles, increasing the mass loading in fact attenuates the turbulence enhancement in most regions (Fig. 7(c)). In Fig. 7(d), it is interesting to note that the extra dissipation term peaks near the side-wall while the extra production term climaxes at a small distance off the axis of symmetry. In general, both terms increase with increasing mass loading.

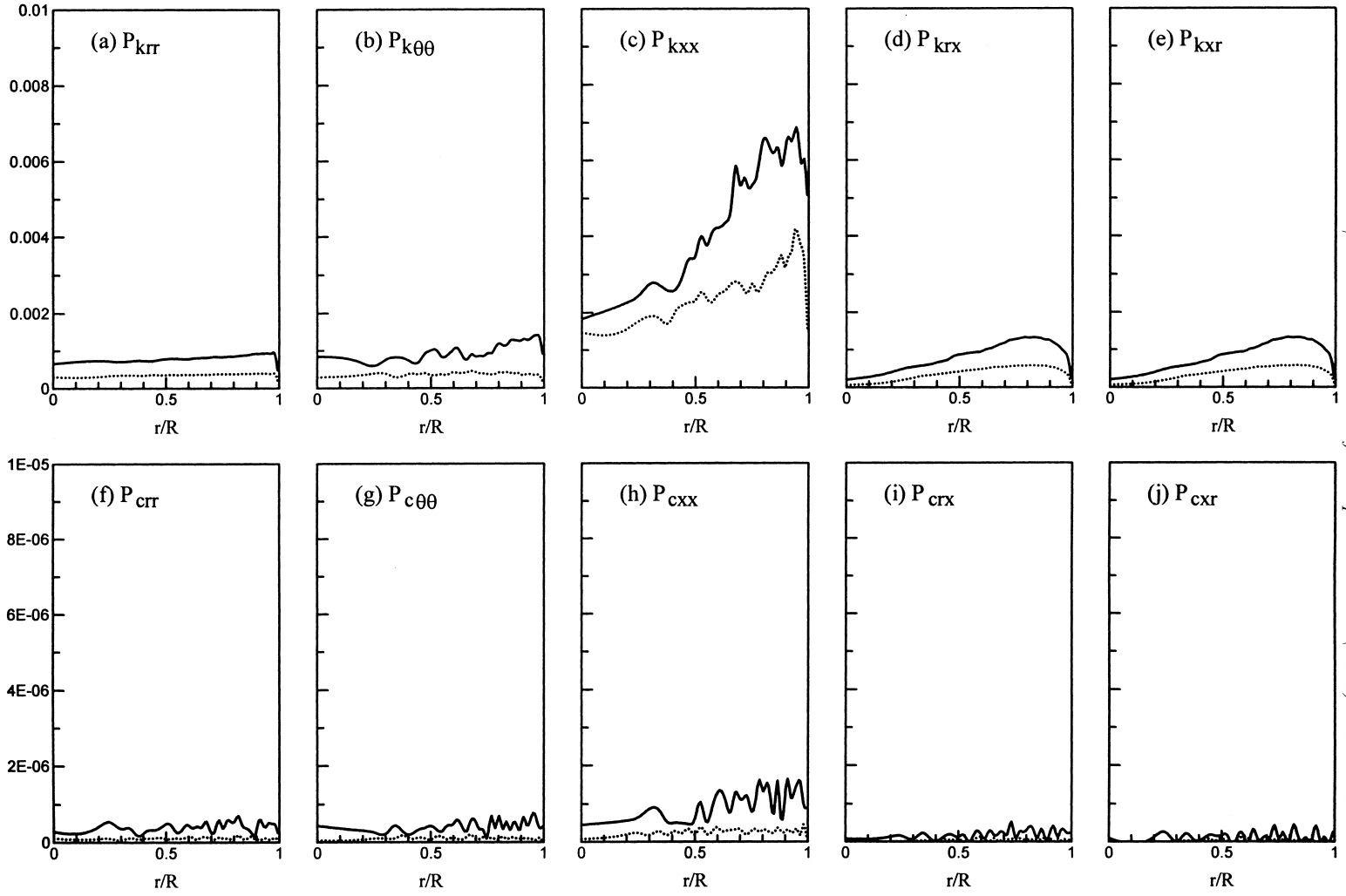

Fig. 11. Variations of solid-phase kinetic stresses, $\boldsymbol{P}_{kij}$ and collisional stresses, $\boldsymbol{P}_{cij}$.

Simulation result for the Reynolds shear stress ($\tau^*_{rx} = \tau_{rx}/(\rho_f U_m^2)$) and the molecular shear stress ($P^*_{frx} = P_{frx}/(\rho_f U_m^2)$) are plotted in Fig. 8. The Reynolds shear stress decreases with increasing mass loading. This obviously is related to the increased dampening of turbulence kinetic energy as shown in Fig. 7(c). In these dilute systems, the effect on the molecular shear stress due to the increase in mass loading is rather insignificant since the alteration of the velocity gradient is only minor (Fig. 7(a)).

Fig. 9(a) shows the variation of solid concentration ($\alpha^*_r = \epsilon_s/\epsilon_m$, where ϵ_m is the bulk solid volume fraction). The solid concentration in average decreases with increasing radius. The mean particle linear velocity ($V^*_x = V_x/U_m$) and the mean particle angular velocity ($\omega^*_{o\theta} = \omega_{o\theta}/(U_m/d)$) are shown in Fig. 9(b) and (c). It is obvious that the no-slip boundary condition does not apply for the solid phase at the side-wall, neither does the zero velocity gradient condition in general. The solid phase slip velocity is determined by an intricate balance of energy and momentum between the solid phase, the fluid phase and the side-wall. This is a challenging problem for theoretical modeling. The same can be said about the mean particle spin. By using numerical simulation, Lun (1996) studied the effect of various solid boundary conditions on macroscopic properties in a single-phase granular Couette flow; for example, translational and rotational velocities, solid concentration, granular temperatures, grain stresses and slip velocity. Similar kind of studies in two-phase flows can likely shed more light on the complicated problem at hand.

The granular translational temperature ($T^*_t = T_t/U_m^2$) and rotational temperature ($T^*_r = T_r/U_m^2$) are plotted in Fig. 10. The granular temperatures are clearly anisotropic. The major component in the translational mode is the streamwise one, T_{tx}, while the one in rotational mode is $T_{r\theta}$. On average, the temperatures increase with increasing radius r.

The distributions of grain kinetic stresses ($\boldsymbol{P}^*_k = \boldsymbol{P}_k/(\rho_f U_m^2)$) and collisional stresses ($\boldsymbol{P}^*_c = \boldsymbol{P}_c/(\rho_f U_m^2)$) are shown in Fig. 11. The anisotropic kinetic stresses are typically about three-order of magnitude larger than the collisional ones in these dilute systems. The kinetic shear stresses are symmetric, whereas the collisional ones are not. Gidaspow and Huilin (1998) recently obtained experimental evidence for the existence of an equation of state for granular particles which is analogous to the ideal gas law for dilute flow. Such an equation, which was predicted by the kinetic theory of granular flows (Lun et al., 1984; Lun and Savage, 1987; Lun, 1991), relates the grain pressure to the granular temperature, solid concentration and particle collisional properties. In passing, it is worthwhile to note that the couple stresses, which arise from the anisotropy of shear stresses, are negligibly small (similar to those obtained by Lun and Liu (1997), hence they are not presented here.

The ratio of the number of particle–particle collisions to the number of particle–wall collisions is plotted against the mass loading in Fig. 12. The simulation result corresponds to that shown in Fig. 1 for pressure gradient. The solid mass flow rate is kept constant at $g_s = 0.03$ kg/s, while the carrier bulk fluid velocity varies. As shown in Fig. 12, the collision ratio increases with increasing mass loading. The number of interparticle collisions can become greater than that of particle–wall collisions even in these dilute flows with solid volume fraction ranging from 0.00234 to 0.00451. Nonetheless, this is not surprising because as demonstrated in the kinetic theory of granular flow (Lun, 1991; Lun and Savage, 1986; Lun et al., 1984), the particle collisional frequency depends not only on the solid concentration but also on granular temperature. In other words, although the concentration might be dilute, if

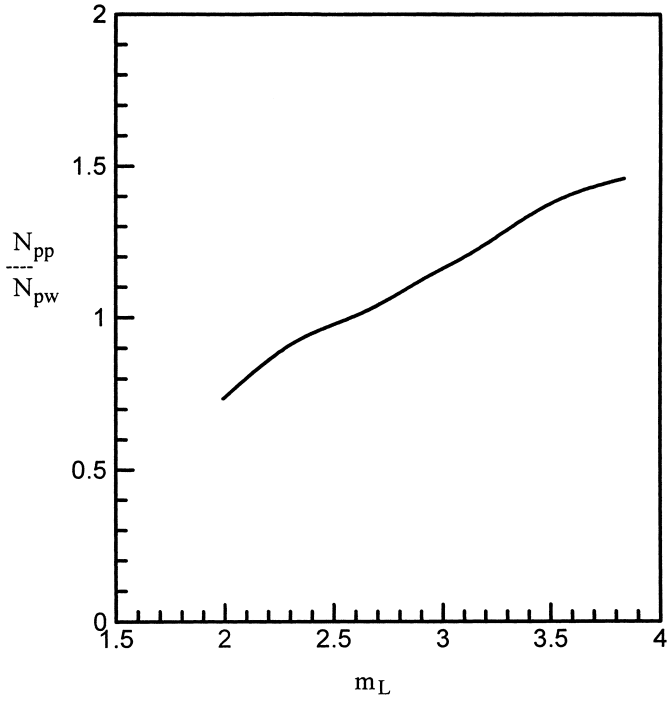

Fig. 12. Ratio of number of particle–particle collisions to number of particle–wall collisions versus mass loading.

the granular temperature is large, the frequency of interparticle collisions can still be relatively high.

8. Conclusion

A new dilute turbulent fluid–solid two-phase model, which incorporates the interfacial couplings in volume fraction, momentum and kinetic energy, and a multiscale k–ω closure, is developed for flows in the grain inertia regime. The model is implemented to simulate air–solid flows in vertical pipes. In general, there is good agreement between the simulation predictions and the experimental measurements for mean fluid and solid velocities, and reasonable qualitative agreement in turbulence intensities. Although the suspensions might be dilute with the solid volume fraction of the order 10^{-3}, the interfacial coupling effects are still significant and should not be ignored. The interfacial force is responsible for modulating the fluid and particle velocity distributions but yet it is not the only factor. The interfacial kinetic energy interactions can influence not only the turbulence kinetic energy distribution but also the fluid and particle velocity distributions. In other words, the mass, momentum and kinetic energy interactions between the fluid and solid phases are intrinsically related as they should be in reality.

Turbulence modulation in fluid–solid two-phase flow system depends crucially on the particle Reynolds number. If the range of particle Reynolds number is smaller than the critical

Reynolds number for flow separation of individual grain, Re_c, then the turbulence field is always attenuated. Such a situation is often encountered in systems with minute and light particles. A combination of turbulence augmentation and attenuation can occur in flow systems where the range of particle Reynolds number encompasses Re_c. However, if the range of particle Reynolds number is greater than the critical Re_p of about 300 for the initiation of vortex shedding, then turbulence enhancement results as a consequence.

The present type of numerical simulation yields many interesting macroscopic flow properties, which are difficult to obtain otherwise. At the same time, it also shows that there is a greater need for experimental verification of these new results now, than ever before. A set of measurements of the kinematic flow properties such as solid concentration, mean fluid and solid velocities, turbulence intensities and granular temperatures, can be very useful in helping better our understanding of the complex two-phase flow problems.

Acknowledgements

This work was partially supported by a research grant from the Natural Science and Engineering Research Council of Canada. The author is grateful to Prof. I.G. Currie for his generosity and hospitality during his sabbatical leave at the Department of Mechanical and Industrial Engineering at the University of Toronto.

References

Clift, R., Gauvin, W.H., 1971. Motion of entrained particle in gas stream. Canadian J. Chem. Eng 49, 439–448.

Crowe, C.T., Troutt, T.R., Chung, J.N., 1996. Numerical models for two-phase turbulent flows. Annu. Rev. Fluid Mech 28, 11–43.

Dennis, S.C.R., Singh, R.N., Ingham, D.B., 1980. The steady flow due to a rotating sphere at low and moderate Reynolds numbers. J. Fluid Mech 101, 257–279.

Elghobashi, S.E., 1994. On predicting particle-laden turbulent flows. Appl. Sci. Res 52, 309–329.

Gidaspow, D., Huilin, L., 1998. Equation of state and radial distribution functions of FCC particles in a CFB. AIChE J 44, 279–293.

Hetsroni, G., 1989. Particles-turbulence interaction. Int. J. Multiphase Flow 15, 735–746.

Jackson, R., 1993. Progress toward a mechanics of dense suspensions of solid particles. AIChE Symp. Ser 90, 1–30.

Lee, S.R., Durst, F., 1982. On the motion of particles in turbulent duct flows. Int. J. Multiphase Flow 8, 125–146.

Lun, C.K.K., 1996. Granular dynamics of inelastic sphere in Couette flow. Phys. Fluids 8, 2868–2883.

Lun, C.K.K., 1991. Kinetic theory for granular flow of dense, slightly inelastic, slightly rough spheres. J. Fluid Mech 233, 539–559.

Lun, C.K.K., Bent, A.A., 1994. Numerical simulation of inelastic frictional spheres in simple shear flow. J. Fluid Mech 258, 335–353.

Lun, C.K.K., Liu, H.S., 1997. Numerical simulation of dilute turbulent gas–solid flows in horizontal channels. Int. J. Multiphase Flow 23, 575–605.

Lun, C.K.K., Savage, S.B., 1987. A simple kinetic theory for granular flow of rough, inelastic, spherical particles. J. Appl. Mech 54, 47–53.

Lun, C.K.K., Savage, S.B., 1986. The effects of an impact velocity dependent coefficient of restitution on stresses developed by sheared granular materials. Acta Mech 63, 15–44.

Lun, C.K.K., Savage, S.B., Jeffrey, D.J., Chepurniy, N., 1984. Kinetic theories for granular flow: inelastic particles in Couette flow and slightly inelastic particles in a general flowfield. J. Fluid Mech 140, 223–256.

Maeda, M., Hishida, K., Furutani, T., 1980. Optical measurements of local gas and particle velocity in an upward flowing dilute gas–solid suspension. In: Proc. Polyphase Flow and Transport Technology (Century 2-ETC, San Francisco), 211–216.

Mei, R., 1992. An approximate expression for the shear lift force on a spherical particle at finite Reynolds number. Int. J. Multiphase Flow 18, 145–147.

Saffman, P.G., 1965. The lift on a small sphere in slow shear flow. J. Fluid Mech 22, 385–400.

Saffman, P.G., 1968. Corrigendum to "The lift on a small sphere in slow shear flow". J. Fluid Mech 31, 624.

Taneda, S., 1956. Experimental investigation of the wake behind a sphere at low Reynolds numbers. J. Phys. Soc. Jpn 11, 1104–1108.

Tsuji, Y., Morikawa, Y., Shiomi, H., 1984. LDV measurements of an air-solid two-phase flow in a vertical pipe. J. Fluid Mech 139, 417–434.

Tsuji, Y., Morikawa, Y., Tanaka, T., Nakatsukasa, N., Nakatani, M., 1987. Numerical simulation of gas–solid two-phase flow in a two-dimensional horizontal channel. Int. J. Multiphase Flow 13, 671–684.

Wu, J.S., Faeth, G.M., 1994. Sphere wakes at moderate Reynolds numbers in a turbulent environment. AIAA J 32, 535–541.

Wilcox, D.C., 1994. Turbulence Modeling for CFD. DCW Industries, Inc.

Yarin, L.P., Hetsroni, G., 1994. Turbulence intensity in dilute two-phase flows. Part III: The particles-turbulence interaction in dilute two-phase flow. Int. J. Multiphse Flow 20, 27–44.

Yuan, Z., Michaelides, E.E., 1992. Turbulence modulation in particulate flows — a theoretical approach. Int. J. Multiphse Flow 18, 779–785.